Materials and Design 95 (2016) 319–328

Contents lists available at ScienceDirect

Materials and Design

journal homepage: www.elsevier.com/locate/matdes

Coupled effect of strain rate and solvent on dynamic mechanical behaviors of separators in lithium ion batteries

Jun Xu [a,b,c], Lubing Wang [a,b], Juan Guan [d], Sha Yin [a,b,c,*]

[a] Department of Automotive Engineering, School of Transportation Science and Engineering, Beihang University, Beijing 100191, China
[b] Advanced Vehicle Research Center, Beihang University, Beijing 100191, China
[c] Beijing Key Laboratory for High-efficient Power Transmission and System Control of New Energy Resource Vehicle, Beihang University, Beijing 100191, China
[d] School of Material Science and Engineering, Beihang University, Beijing 100191, China

ARTICLE INFO

Article history:
Received 30 September 2015
Received in revised form 16 December 2015
Accepted 9 January 2016
Available online 26 January 2016

Keywords:
Battery separator
Mechanical property
Anisotropy
Strain rate effect
Viscoelasticity

ABSTRACT

Mechanical properties of separators have a great impact on the electrochemical performance of lithium ion battery, such as capacity, charge/discharge behavior, charging cycles and among others. In the present study, two typical widely commercialized separators, Celgard 2400 and Celgard 2340, are the investigation objects with single layer and three-layer structures respectively. Firstly, to investigate material anisotropy and strain rate effects, tensile tests conducted on MTS and Instron at various strain rates from 0.01 to 50 s^{-1} are carried out with samples prepared at three different directions: transverse direction (TD, 0°), machine direction (MD, 90°) and 45°. The failure strain decreases while failure stress increases with the strain rate for materials in all three directions. Material anisotropy is observed within the porous structure with nanofiber reinforced in the polymer matrix. Secondly, the environmental solvent effect is also examined: dimethyl carbonate (DMC) solution has a negative effect on the mechanical property of the separator while water may exert a positive effect. Furthermore, DMA Q800 is employed to study the viscoelasticity of separators at various temperatures and frequencies. A simple viscoelastic model based on Kelvin–Voigt model is proposed for the two types of separators. This research may serve as a solid step towards the comprehensive understanding of LIB separator and shed light on the future research of unveiling physical relation between mechanical properties and electrochemical performance of LIB.

1. Introduction

Generally, the current widely commercialized separator in lithium-ion batteries (LIBs) is a type of porous polymer material placed between cathodes and anodes to separate the two electrodes and thus to avoid short circuit while providing channels for the transportation of lithium ions [1–5]. Separators usually consist of a polymeric membrane with one or multiple microporous layers [2,3] and they are required to be chemically and electrochemically stable as well as mechanically robust during the electrochemical reaction [6]. Regarding the mechanical properties, the separator should be strong enough to withstand the possible tension and compression of winding operation during LIB assembling [1]. Catastrophic consequences could follow with the failure of the battery separator such as short circuits, fires and even explosions [7]. Moreover, mechanical failure or deformation of separator is critical for evaluating the electrochemical performances including cell life and capacity degradation [8]. Therefore, mechanical properties of the separator have attracted much research attention with respect to the LIB safety. Previous studies have mainly focused on the essential properties of the separator such as porosity [1,2,9–11], pore size [1,2], thickness [1,2], chemical stability [1,2,12], permeability [1,2], mechanical strength [1,2,8,9,12], wettability [1,2,13,14], thermal stability [1,2,9] and thermal shutdown [1,2,9], and which factors dominate are also discussed. A comprehensive and detailed review can be referred to Ref [1,2]. On the other hand, other researches [15–18] investigated the fabrication process with various composite materials and the physical, electrochemical, and thermal properties of some new materials were thoroughly discussed. Moreover, the composite polymer with various fillers as inert ceramic oxides (SiO_2 and TiO_2), ferroelectric material (Al_2O_3), super acid oxides, Nunes-Pereira et al. [19], single polymers, composites and polymer blends based on PVDF and its copolymers [20], whose main properties were summarized and compared with corresponding pristine polymer to find a method of increasing the performance. Well-designed experiments to explore the mechanical properties of the separators were reported in 2011 by Xiao et al. [8]. They conducted creep and frequency sweep experiment on single layer polypropylene separator and discovered the anisotropy of the separator due to the complexity of the material itself with oriented reinforcement fibers. To study the mechanical behaviors of the separator under compression, Arnold et al. [21] designed compression tests with

* Corresponding author at: Department of Automotive Engineering, School of Transportation Science and Engineering, Beihang University, Beijing 100191, China.
E-mail address: shayin@buaa.edu.cn (S. Yin).

http://dx.doi.org/10.1016/j.matdes.2016.01.082
0264-1275/

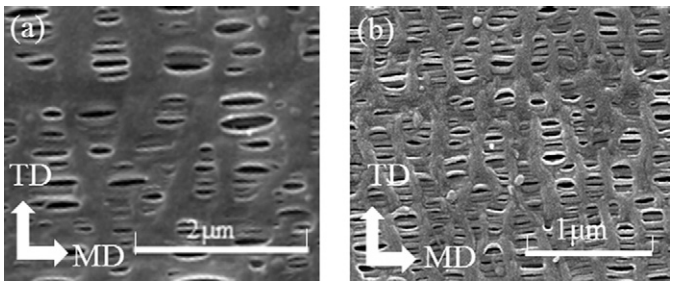

Fig. 1. Field emission scanning electron microscope image of (a) Celgard 2400 and (b) Celgard 2340.

Table 1
Experiment designs for coupling of strain rate, anisotropy and environment solvent of Celgard 2400 and Celgard 2340.

Experimental types	Environment	Direction (°)	Strain rate (/s) loading stress (MPa)
Quasi-static	Dry	0/45/90	0.01/0.1/1
	Water	0/45/90	0.01/0.1/1
	DMC	0/90	10/50
Dynamic	Dry/water	0/45/90	10/50
Frequency scan	Dry	0	Scanning frequency 0.01–100 Hz
Temperature scan	Dry	0	Scanning temperature −120 °C–120 °C
Creep	Dry	0	10/20/40

multiple layers of sample stacking and studied the mechanical behaviors at low strain rates. More research has concentrated on the influence of solvent [3,22] to reproduce the effect of the actual environment for the LIB separator. Chen [23] explored LIB's failure and safety that is associated with the mechanical behavior of separators. It was discovered that LIB's capacity is attenuated under compression with the influence of the closed pores of the separator. Recently, Yan et al. [24] explained the influence of environment solvent on the separator on a molecular scale using molecular dynamics simulation.

These pioneering investigations lay a concrete foundation for us to understand the mechanical behaviors of the separators made from specific materials at ambient conditions. However, the dynamic mechanical behaviors [25] of the separator still remain blank whereas the battery mechanical integrity usually fails [26,27]. Furthermore, the strain rate effect under ambient conditions and the anisotropy in both mechanical properties and morphologies need to be studied. This would help us to completely resolve the mechanical responses of the separator under dynamic loadings [28], e.g., vibrations or impacts which would accelerate the degradation of electrochemical performance, and on the other hand, the description of mechanical behavior at extreme loading conditions of LIB as a whole remains unsolved. Therefore, the current study mainly focuses on the investigations of the dynamic mechanical behaviors of the separator. Dynamic strain rates from 0.01/s to 50/s are chosen and mechanical properties from stress–strain curves are analyzed. Furthermore, the anisotropy and environment solvent effects are also considered, and are coupled with the effect of strain rate. This may reveal the mechanical behaviors in a more realistic way. Finally, the viscoelasticity of the separator are studied with temperature and frequency scanning sweep experiment on a DMA Q800 machine. The acquired information may help to build a deep understanding of mechanical behaviors of the separator and the corresponding LIB performance.

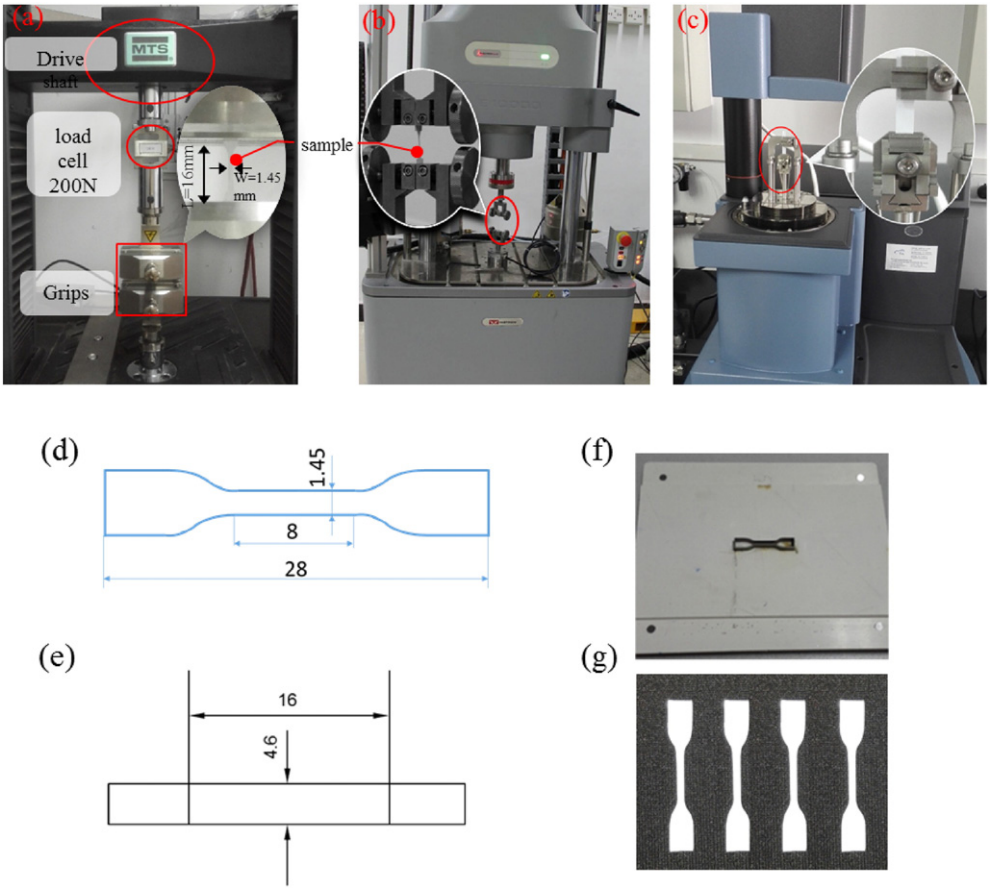

Fig. 2. (a) MTS criterion for quasi-static tensile test; (b) Instron E10000 for dynamic tensile test; (c) DMA Q800 for dynamic mechanical test; (d) the sample dimension of tensile test [30]; (e) the sample dimension of DMA; (f) Cutting tool; (g) the samples cut by cutting tool.

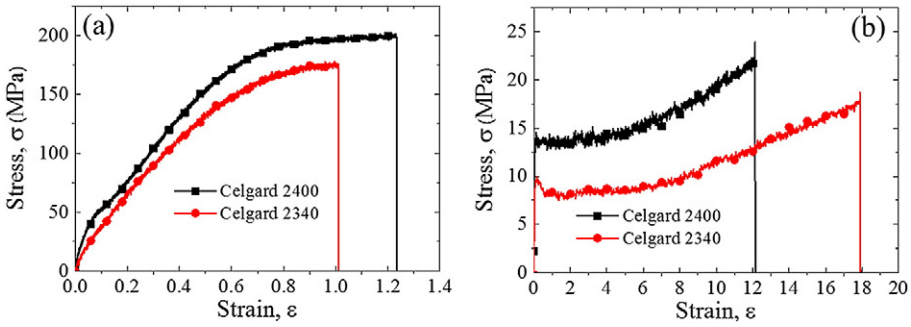

Fig. 3. Contrast stress–strain curve in dry condition with the strain rate of 0.01/s of two separators in (a) MD; (b) TD.

2. Experiment

2.1. Materials

Celgard 2400 and Celgard 2340 (Celgard, LLC) as two typical separators in LIB were selected in the present study. Celgard 2400 is a single-layer polypropylene (PP) separator of 20 μm thick, and Celgard 2340 is a three-layer PP/PE (polyethylene)/PP composite separator of 38 μm thick. Field emission scanning electron microscope (FESEM) Quanta 200F was used to investigate the microstructure of the two separators as shown in Fig. 1. Based on the distinct porous microstructure, 0° direction as machine direction (MD) and 90° direction as transverse direction (TD) are defined throughout the study.

2.2. Methods

A series of mechanical tests are designed by coupling the effects of strain rate, material anisotropy and environment solvent, as summarized in Table 1. Samples at different strain rates ranging from 0.01/s to 50/s along 0° (MD), 90° (TD), and 45° directions are tested to explore the coupled effect of material anisotropy and strain rate. Dry in air, wet in water and wet in dimethyl carbonate (DMC) conditions are chosen to investigate how the solvent influences the mechanical behaviors of the separator. For dry conditions, samples are kept dry as obtained and the humidity of the ambient environment is about 40%. For wet conditions, samples are immersed in water or DMC solvent for up to 48 h to ensure the materials are saturated. The samples in tensile test are designed according to ASTM D638 testing standard for polymer material tension (Fig. 2(d)) and DMA testing (Fig. 2(e)), and prepared by a custom-made sharp cutter (Fig. 2(f)) that aims to reduce the flaw introduction. MTS E44 is employed to investigate the mechanical behaviors of the separators at quasi-static to low strain rate loadings, i.e., strain rates of 0.01 to 1 s^{-1} with a load sensor of 200 N and accuracy of 0.001 N, shown in Fig. 2(a). Samples are fixed at two ends using specially designed fixtures for thin films. Instron E10000 (Fig. 2(b)) is used for the higher strain rate measurements, i.e., strain rates from 10 to 50 s^{-1}.

DMA Q800 machine (Fig. 2(c)) is employed for dynamic mechanical measurements to analyze storage modulus (E'), loss modulus (E'') and tangent delta ($\tan\delta$) under temperature and frequency sweep conditions. In the temperature ramping experiment, the setting parameters are: frequency of 1 Hz, a constant amplitude of 20 μm, a linear heating rate of 3 °C/min. Frequency from 0.01 to 50 Hz at room temperature is

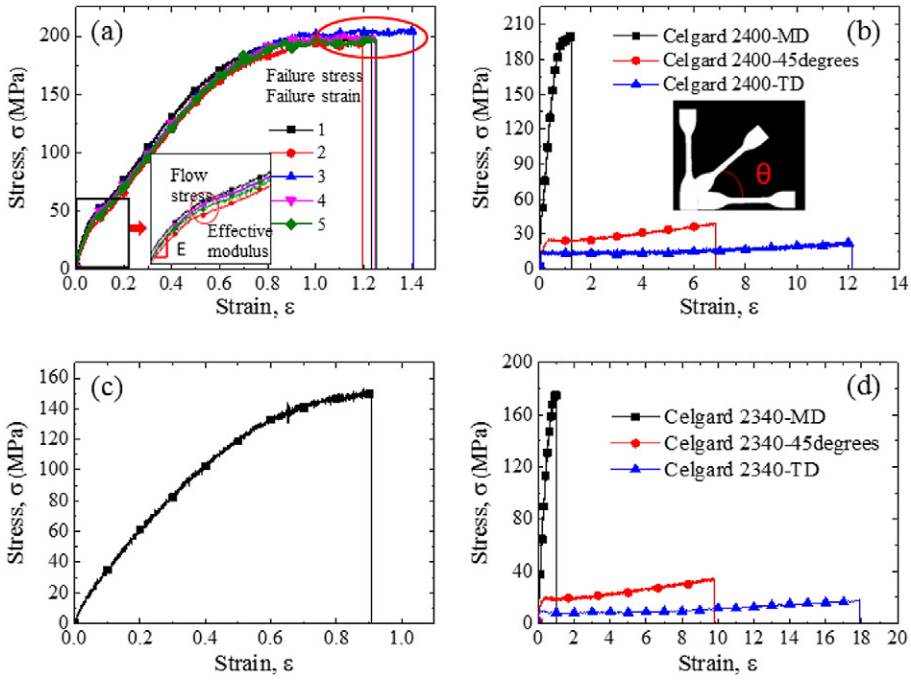

Fig. 4. (a) The tensile stress–strain curves with strain rate 0.01/s of Celgard 2400 at MD; (b) stress–strain curves of Celgard 2400 under different directions; (c) the tensile stress–strain curves with strain rate 0.01/s of Celgard 2340 at MD; (d) stress–strain curves of Celgard 2340 under different directions.

chosen in the frequency sweep experiment. Meanwhile, creep tests are carried out to quantify the viscoelastic properties of the separator. The sample shape in dynamic mechanical tests is simply rectangular as shown in Fig. 2(e) with 4.6 mm in width and clamp distance (effective length) of about 16 mm.

3. Results and discussion

3.1. Material effect

Comparison of the material between the two separators under dry, ambient conditions is shown in Fig. 3. Celgard 2400 has larger effective modulus and failure stress than Celgard 2340 along both MD and TD, and the failure strain is larger in MD for both separators while smaller in TD. There could be two reasons for this phenomenon. Firstly, tensile modulus and the tensile strength of PP ($E = 1.4$ GPa, $\sigma_f = 33$ MPa) are better than those of PE ($E = 1.07$ GPa, $\sigma_f = 20$ MPa,) while as the toughness (elongation at break $\varepsilon_f = 150\%$ for PP, $\varepsilon_f = 1200\%$ for PE) is smaller. Secondly, three-layer structure of Celgard 2340 may have weak interfacial strength.

3.2. Anisotropy

For large deformation tensile experiment, all the tests listed in Table 1 are repeated for 4–5 times under the same condition to ensure the reliability of the experimental data. Fig. 4(a) shows the repeated tensile tests for Celgard 2400 along MD direction at strain rate of 0.01 s^{-1} and the stress–strain curves are highly overlapped. Representative stress–strain curves at three different angles show strong material anisotropy, as illustrated in Fig. 4(b). The stress–strain curves for samples prepared along MD direction display a rather strong nonlinearity while as samples cut along TD direction show an obvious plasticity enhancement after the strain reaches 0.1. We define effective Young's modulus E as the slope of the initial linear region shown in the subplot of Fig. 4(a), and then get $E_{MD} = 659$ MPa and $E_{TD} = 253$ MPa. The failure strain ε_f for samples from MD and TD directions are also different with $\varepsilon_{MD} \approx 1.2$ and $\varepsilon_{TD} \approx 12$. Materials' property is dominated by the mechanical behavior of nanofibers along MD direction; and polymer matrix is dominating along TD direction, since nanofibers align mostly along MD direction within the samples. Along 45 degrees direction, the samples exhibit balanced mechanical properties from MD and TD directions. Celgard 2340, as shown in Fig. 4(c) and (d), shows similar material anisotropy with $E_{MD} = 528$ MPa and $E_{TD} = 167$ MPa, the failure stress $\sigma_{MD} = 164$ MPa, $\sigma_{TD} = 17.7$ MPa and the failure strain $\varepsilon_{MD} = 0.9$, $\varepsilon_{TD} = 17.4$.

Thus, it is necessary to consider separators' anisotropy while winding during LIB assembling, i.e., MD is a good winding direction for its higher strength.

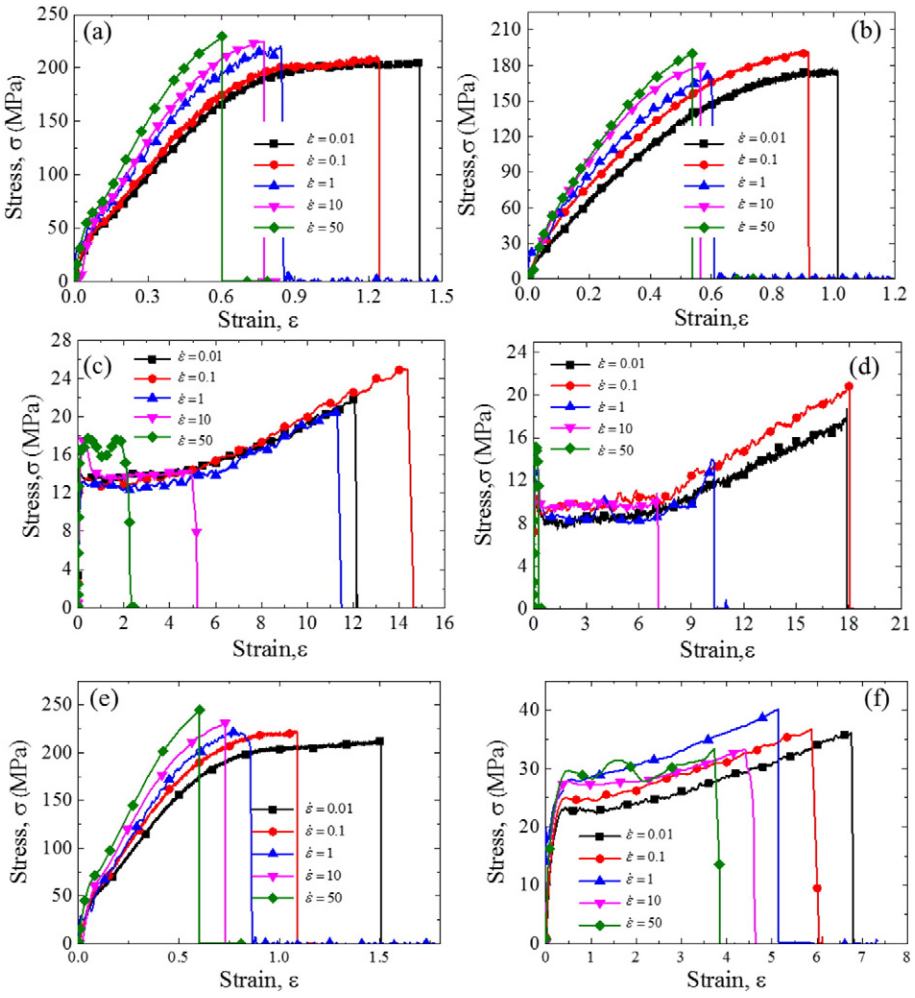

Fig. 5. Stress–strain curves under different strain rates (a) Celgard 2400 in MD with dry condition; (b) Celgard 2340 in MD with dry condition; (c) Celgard 2400 in TD with dry condition; (d) Celgard 2340 in TD with dry condition; (e) Celgard 2400 in MD with water condition; (f) Celgard 2340 in MD with water condition; (g) Celgard 2400 in TD with water condition; (h) Celgard 2340 in TD with water condition; (i) Celgard 2400 in MD with DMC condition; (j) Celgard 2340 in MD with DMC condition; (k) Celgard 2400 in TD with DMC condition; (l) Celgard 2340 in TD with DMC condition.

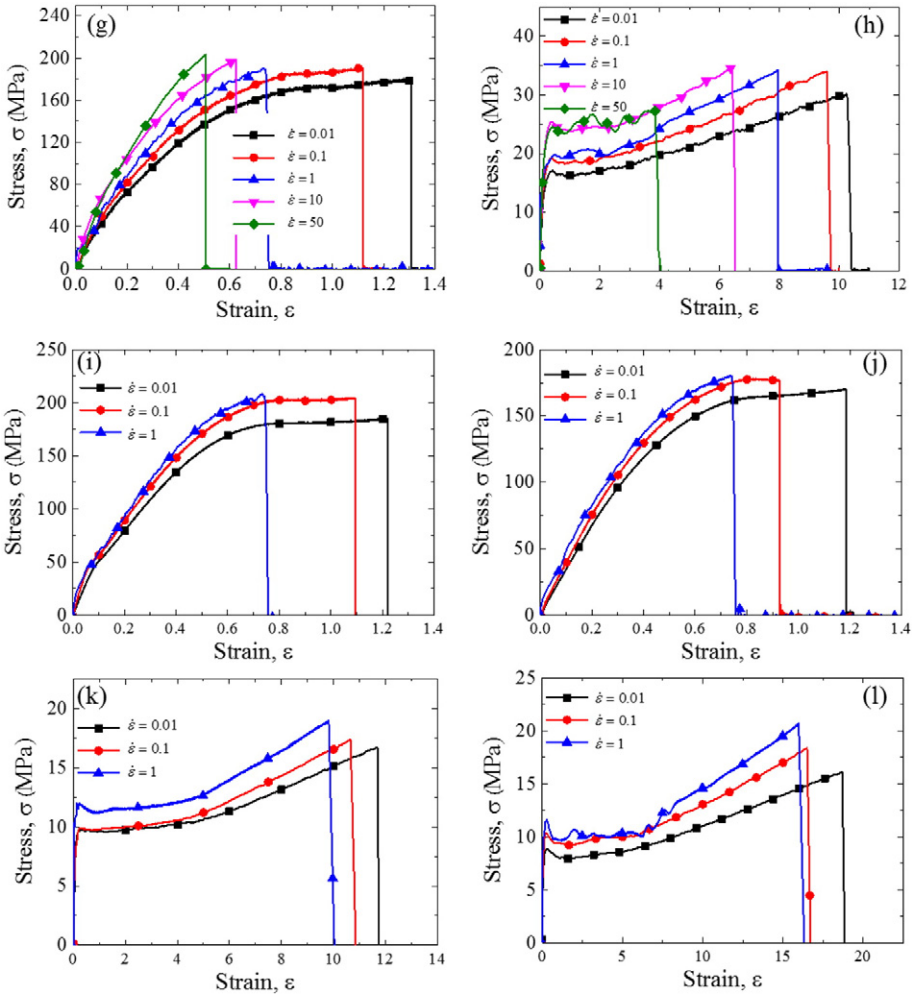

Fig. 5 (*continued*).

3.3. Strain rate effect

Fig. 5 shows the representative stress–strain curves under different strain rates varying from 0.01 to 50 s^{-1}. Fig. 5(a) and (b) are the curves in MD under dry condition for both Celgard 2400 and Celgard 2340, which present different slopes under different strain rates. The flow stresses σ_s and the failure stress σ_f increase with the strain rate, which shows a typical strain-hardening phenomenon. At low strain rate of 0.01/s, the curve for Celgard 2400 along MD shows plasticity when the strain reaches 0.9 while that along TD behaves elastically at high strain rate of 50/s. Besides, the failure strain ε_f decreases with the strain rate: strain at low strain rate $\varepsilon_{f\_low} \approx 140\%$, is almost twice as strain at high strain rate $\varepsilon_{f\_high} \approx 60\%$ for Celgard 2400 along MD. Similarly, in Celgard 2340, $\varepsilon_{f\_low} \approx 100\%$ *and* $\varepsilon_{f\_high} \approx 50\%$ are the strains at low and high rate respectively. The curves for samples (Fig. 5(e) and (f)) under water and (Fig. 5(i) and (j)) under DMC wet conditions for the two materials show similar characteristics as that under dry conditions.

Along TD, the curves under dry condition also exhibit strain rate effect as shown in Fig. 5(c) and (d), and the performance differs strongly under quasi-static and dynamic conditions. The failure strain ε_f under dynamic loading is about 400%, much smaller than that under quasi-static tensile test with $\varepsilon_f \approx 1400\%$. The curves under water and DMC conditions as shown in Fig. 5(g), (h), (k), and (l) exhibit similar tendency to that under dry conditions.

The separators have obvious strain rate effect, its strength become higher with higher strain rate, which makes sense in impact protection and should be an advantage in designing a new battery.

3.4. Solvent implication

The dominant parameters, effective Young's modulus E, fracture stress σ_f, under dry, water wet and DMC wet conditions, are extracted from typical stress–strain curves, respectively. As Fig. 6(a)(d) shown, linear trends are fitted, E and σ_f along MD with samples immersed in water are larger than those under dry conditions. In other words, the stiffness of the separator immersed in water is better than that in dry conditions. Recent simulation results revealed that DMC molecules would penetrate into the amorphous nanofiber, reducing local density and Young's modulus of the sample; on the contrary, as a polar solvent water would probably have an opposite effect to enhance Young's modulus of the amorphous nanofiber [24]. This explanation could stand for single layer PP (Celgard 2400) and composite layer of PP/PE/PP (Celgard 2340). As shown in Fig. 6(e)–(h), the failure stress σ_f as for two separators in water are larger than that in DMC along both MD and TD.

3.5. Coupled effects

Fig. 7 shows the curves with error bar about typical parameters of mechanical properties (modulus, failure stress) under coupled effects from materials, strain rates, environmental conditions and intrinsic anisotropy.

As shown in Fig. 7(a), modulus variations for the two separators at different conditions are summarized. The slope of curves in magenta and red is larger than that in blue and black, which means the separator

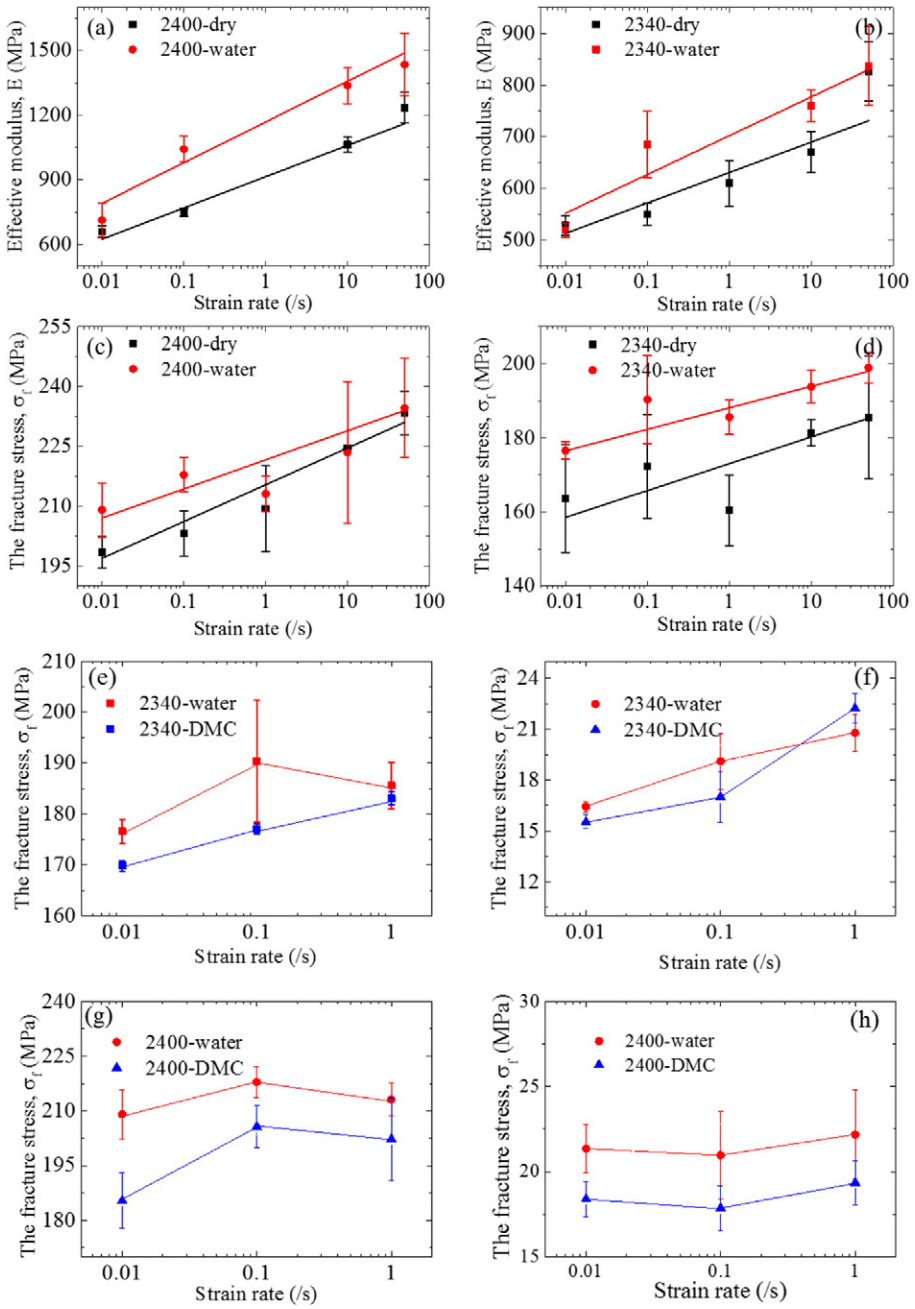

Fig. 6. The effective modulus-strain rate curve under dry and water condition in MD (a) Celgard 2340; (b) Celgard 2400; the fracture stress–strain rate curve under dry and water condition in MD (c) Celgard 2340; (d) Celgard 2400; the fracture stress–strain rate curve under water and DMC condition (e) Celgard 2340 in MD; (f) Celgard 2340 in TD; (g) Celgard 2400 in MD; (h) Celgard 2400 in TD.

shows stronger strain rate effect in water condition compared to dry condition. This may be caused by the strain-rate dependence of the aggregation behaviors of water molecules surrounding the nanofibers. Similarly, the effective modulus of Celgard 2400 has more obvious strain rate dependence than that of Celgard 2340, and the effective modulus enhanced more under water condition than Celgard 2340 as the curve differ more obviously under dry and water conditions.

The failure stress σ_f of the separator with coupled conditions are shown in Fig. 7(b). The strain rate effect on failure stress is less obvious than that on effective modulus in both MD and TD. Additionally, the strain rate effect along MD is stronger than that along TD; and when immersed in water and DMC, σ_f in MD changes even more than that along TD. As for material types coupled with solvent, the failure stress becomes larger in water and the effect on Celgard 2340 is larger than that on Celgard 2400. As shown in Fig. 7(c), the failure strain along TD decreases slowly at quasi-static strain rate, as decreases sharply in dynamic tests. The failure strain along TD at strain rate 50/s is close to that along MD, which can be well explained by the strain rate induced brittlement.

3.6. Temperature and frequency sweep dynamic mechanical testing

For Celgard 2400, the storage modulus declines while the loss modulus increases at first then decreases as well as tan delta with the temperature and has a peak at about 5 °C and 13 °C respectively as shown in Fig. 8(a). For Celgard 2340, as shown in Fig. 8(b), there is a small turning point of tan delta at about −121.38 °C as a secondary structural relaxation, which is considered as β-relaxation (an amorphous phase relaxation) [15]. Also, the storage modulus falls sharply at the temperature range from −11 °C to 20 °C, namely the glass

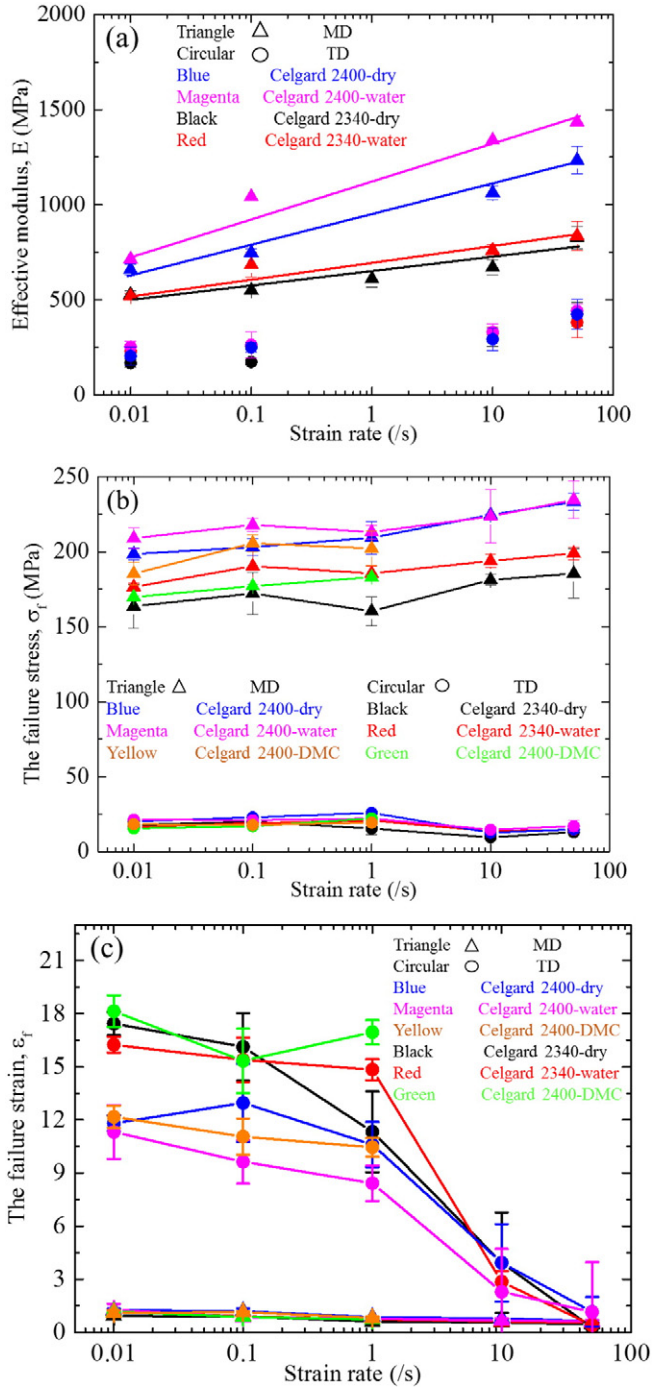

Fig. 7. Curves with error bar under different materials, environment and directions (a) effective modulus-strain rate curve; (b) the failure stress–strain rate curve; (c) the failure strain–strain rate curve.

transition zone, accompanied with the increase of tan delta with peak located at 13.93 °C, followed by a new loss-peak which could not complete. Therefore, another supplementary temperature scanning test ranging from room temperature to 150 °C is further conducted as shown in Fig. 8(e), with another peak appearing at around 85.39 °C, and the sample failed at its melting point of about 135 °C (Fig. 8(f)). According to the characteristics above of the dynamic mechanical properties, the glass transition zone of Celgard 2340 which is caused by α-relaxation of PP, should be from −15 °C to 20 °C. There is a loss-peak between the glass transition zone and the melting point which is suggested as the relaxation of the oriented amorphous structure (meta-order). This is an intermediate structure between the long range order arrangement of crystals and non-crystalline disordered arrangement, which relaxes as subjected to mechanical stress and above the glass transition conditions. As illustrated, the glass transition temperatures of two separators are both within the range of daily use temperature, and its storage modulus decreases sharply during glass transition. Thus, the separator in low and high temperature may have different mechanical properties which is not stable in use.

Comparing the results of two temperature ramp experiments as shown in Fig. 8(e), the tan delta profile differs at the high temperature region obviously. One reason could be the sample heterogeneity, namely the sample for the first temperature sweep from −150 °C to 70 °C has higher amorphous orientation in molecular structure. Another reason could be that in the second experiment the sample is heated up directly from room temperature so that the amorphous structure of the sample doesn't have enough time to relax completely, which in turn is added to the meta-order relaxation.

For frequency sweep experiment as shown in Fig. 8(c) and (d), the storage modulus increases with the frequency and can be correlated linearly with log (frequency) for both separators. On the other hand, the loss modulus and tan delta have a valley at different frequencies. At room temperature, the material finishes glass transition and that's the reason why the sample has strong frequency dependence.

3.7. Creep responds and the viscoelastic constitutive model

To further investigate the viscoelasticity of the separators, a series of creep tests are performed in the MD under dry condition. Samples are loaded for 60 min and relaxed for another 60 min for unloading. Note that preliminary experiments have proven such time period was long enough for samples to get to equilibrium. The results are shown in Fig. 9(a) and (b). Creep recovery is not performed for higher stress than 40 MPa because the load is very large and the sample is plastically deformed.

As shown in Fig. 9(a) and (b), the strain rises rapidly in the first few seconds and then changes slowly with creep rate decreasing with time. For the recovery part, the strain decreases in an instant followed with a slow recovery without full recovery at the end of the experiment. The larger the stress is applied, the larger the unrecovered strain is.

The elastic structure responds instantaneously and the viscous structure changes slowly as a function of time. A five Kelvin–Voigt elements model is used to describe the viscoelasticity of the separator as shown in Fig. 9(c). The springs and dashpots represent the elastic and viscous parts of the material respectively.

The Kelvin–Voigt model can be described mathematically as [29]

$$J(t) = J_0 + \sum_{i=1}^{5} J_i\left(1 - exp\left(\frac{-t}{\tau_i}\right)\right) \quad (1)$$

where J_0 is the instantaneous compliance; J_i is the creep constant and τ_i is the retardation times associated with Kelvin–Voigt element i and i = 1,2,3,4,5.

The stress–strain function could be rewritten as [8]

$$\sigma(t) = \int_{-\infty}^{t} G(t-s)\frac{d\varepsilon(t)}{dt}ds. \quad (2)$$

Modeling fittings are provided in Fig. 9(d) and (e) based on Kelvin-Voigt model. The parameters are summarized in Table 2 for all cases. Now, it is pretty convenient to employ the above suggested models to for applications.

Moreover, the sensitivity study has been conducted. The current research tuned each variable to its ±10% value range based on the optimal fitting results, and draws the curve with error bars. Take the Celgard 2340 under 10 MPa loading as example, the sensitivity of different variables is analyzed. The effect of creep constant J_i is larger than

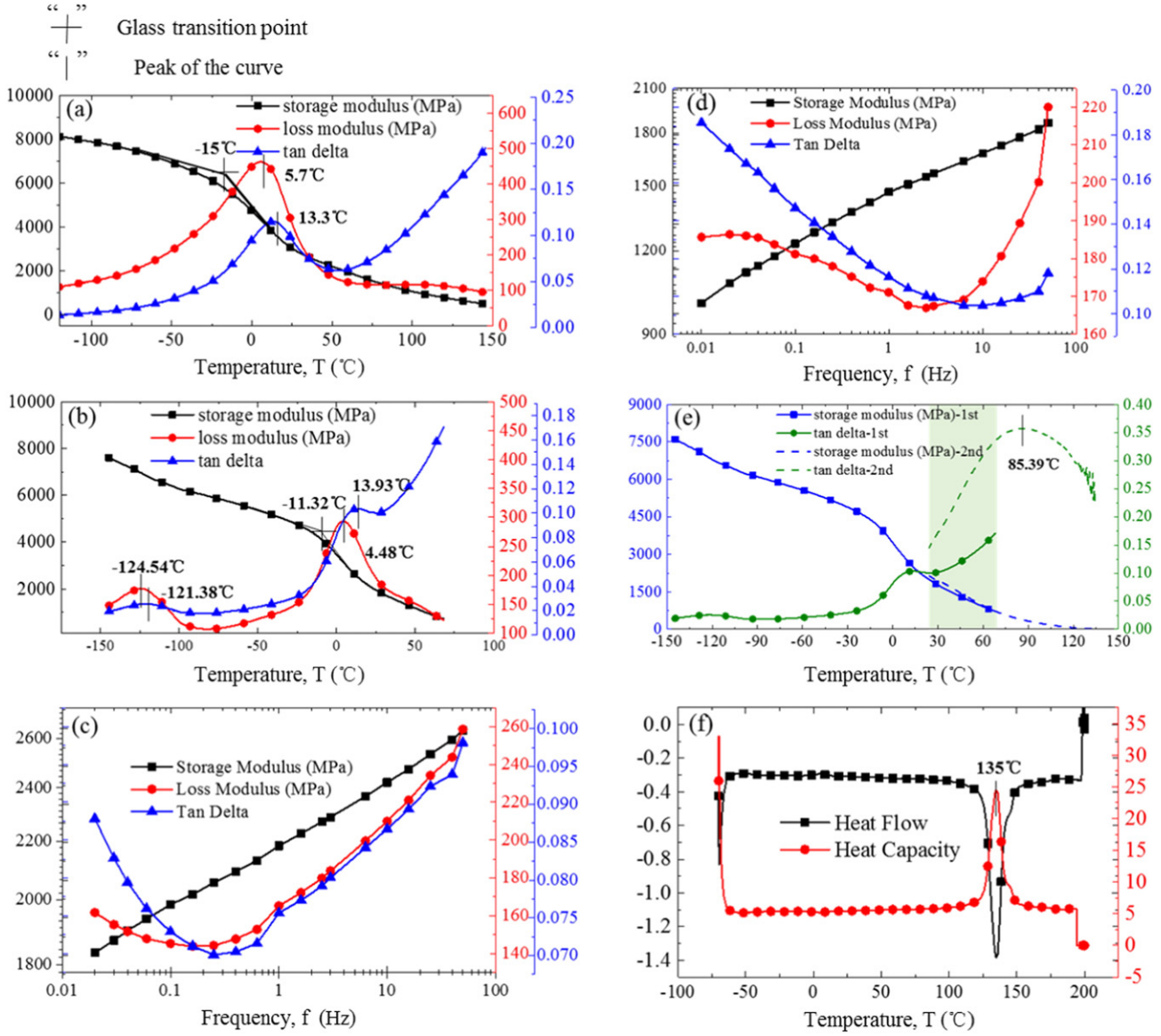

Fig. 8. (a) Temperature scan results of Celgard 2400 at frequency of 1 Hz; (b) temperature scan results of Celgard 2340 at frequency of 1 Hz; (c) frequency scan results of Celgard 2400 at room temperature; (d) frequency scan results of Celgard 2340 at room temperature; (e) contrast curves of two temperature scan tests under different ranges of temperature of Celgard 2340; (f) DSC test of Celgard 2340.

that of retardation times τ_i, as shown in Fig. 10(a) and (b) (without loss of generality, J_4 and τ_3 are compared) which shows the largest effect variable among different τ_i and J_i respectively.

4. Concluding remarks

LIB separator serves as the core building blocks of lithium-ion battery and ensures the transient and long-term electrochemical performance. In this paper, the mechanical properties of two typical separators were thoroughly investigated with the focus on the dynamic mechanical performances. Firstly, the anisotropy was found by testing of materials prepared from various directions, and explained by manufacturing method and FESEM images. The tensile stress–strain curve was measured under different stain rates varying from 0.01 to 50 s^{-1}, and the separators were proven to be highly strain rate dependent in all directions. Besides, the effect of solvent where the separators were saturated was studied, and water was shown to strengthen the separators whereas DMC softened the separators. Furthermore, the glass transition temperature was obtained from the temperature ramp experiment conducted on DMA Q800,and the storage modulus decreased with temperature and has a frequency-dependence. Finally, creep tests were performed to investigate its viscoelasticity, and a mathematical viscoelastic model was proposed for engineering application. The results may shed light on the comprehensive understanding of the complicated mechanical behaviors of separators, facilitating engineering design and fabrication for proper LIB separators.

Acknowledgments

JX would like to thank the financial support of Fundamental Research Funds for the Central Universities, Beihang University and the startup fund for “Zhuoyue 100” titled professor, Beihang University. GJ would like to thank the startup fund for “Zhuoyue 100” titled associate professor from Beihang University. SY would like to thank the financial support from Natural Science Foundation of China (No. 11402012).

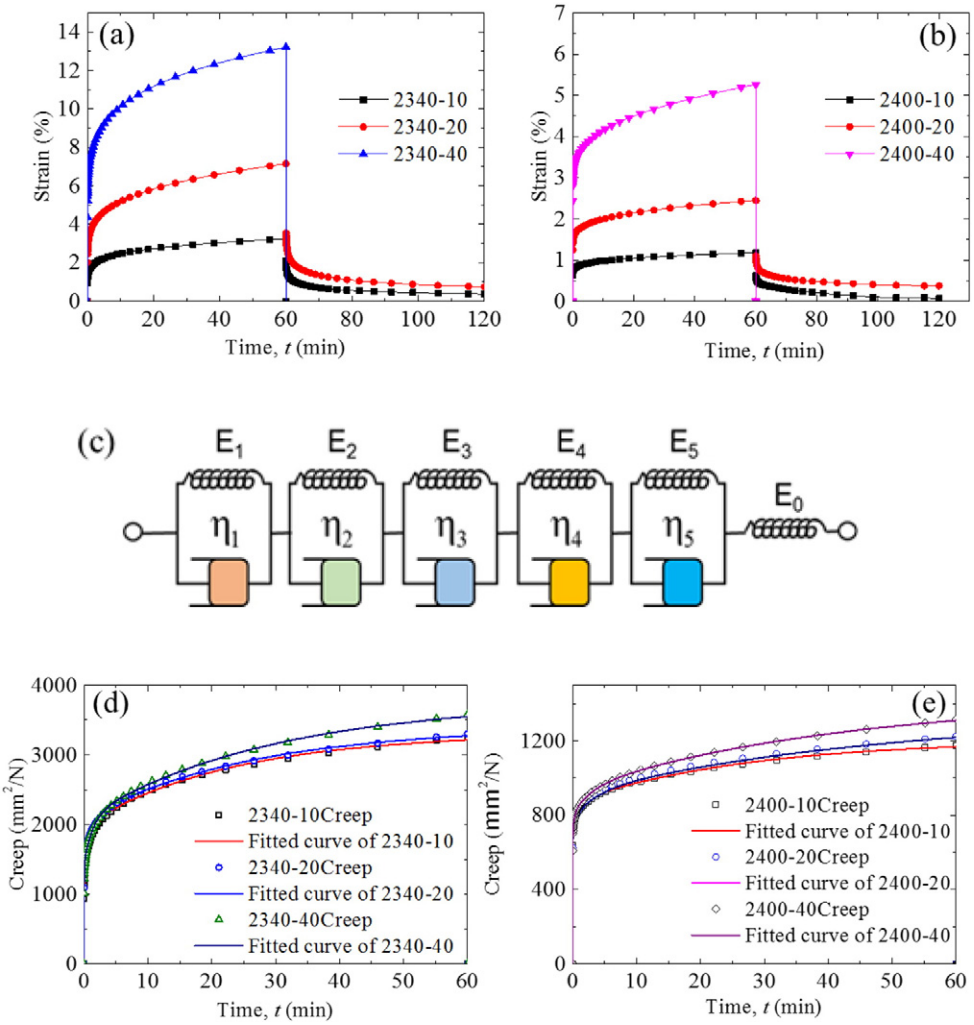

Fig. 9. (a) Creep results of Celgard 2340; (b) Creep results of Celgard 2400; (c) schematic diagram of Kelvin linear viscoelastic model [8]; (d) fitting curves of Celgard 2340; (e) fitting curves of Celgard 2400.

Table 2
Fitting data of two separators with different loading stresses.

Celgard 2340	10 MPa	20 MPa	40 MPa	Celgard 2400	10 MPa	20 MPa	40 MPa
J_0	4.162e−05	267.5	241.2	J_0	155.1	203.3	2.22e−14
J_1	422.5	267.3	241.6	J_1	155.3	268.5	95.43
J_2	1325	237.2	1677	J_2	191	202.5	130.5
J_3	1170	591.3	704.4	J_3	335.7	138.4	492.1
J_4	4.158e−05	1321	258.6	J_4	241.7	385.4	2.22e−14
J_5	590	725.9	645.2	J_5	127.8	62.78	709.4
τ_1	19.45	0.03219	0.05938	τ_1	0.003225	1.214	17.2
τ_2	2213	0.03445	1764	τ_2	2.22e−14	0.001267	171.7
τ_3	1.164	75.15	3.007	τ_3	1641	64.75	2503
τ_4	0.0326	1576	2.22e−14	τ_4	1.264	1670	0.06235
τ_5	175.2	2.645	82.45	τ_5	71.1	0.0274	0.8918

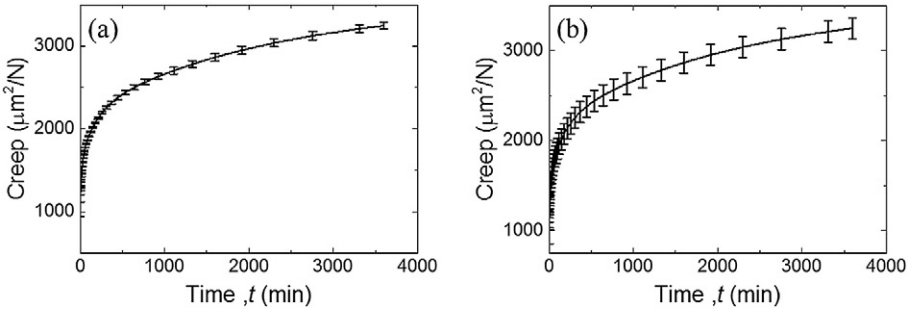

Fig. 10. Fitting curves with error bar with the sensitivity study of: (a) retardation times τ_3; (b) creep constant J_4.

References

[1] H. Lee, M. Yanilmaz, O. Toprakci, K. Fu, X. Zhang, A review of recent developments in membrane separators for rechargeable lithium-ion batteries, Energy Environ. Sci. 7 (2014) 3857–3886.
[2] S.S. Zhang, A review on the separators of liquid electrolyte Li-ion batteries, J. Power Sources 164 (2007) 351–364.
[3] G.Y. Gor, J. Cannarella, C.Z. Leng, A. Vishnyakov, C.B. Arnold, Swelling and softening of lithium-ion battery separators in electrolyte solvents, J. Power Sources 294 (2015) 167–172.
[4] X.S. Huang, Separator technologies for lithium-ion batteries, J. Solid State Electrochem. 15 (2011) 649–662.
[5] Y. Lee, H. Lee, T. Lee, M.-H. Ryou, Y.M. Lee, Synergistic thermal stabilization of ceramic/co-polyimide coated polypropylene separators for lithium-ion batteries, J. Power Sources 294 (2015) 537–544.
[6] P. Arora, Z. Zhang, Battery separators, Chem. Rev. 104 (2004) 4419–4462.
[7] C.-Y. Jhu, Y.-W. Wang, C.-M. Shu, J.-C. Chang, H.-C. Wu, Thermal explosion hazards on 18650 lithium ion batteries with a VSP2 adiabatic calorimeter, J. Hazard. Mater. 192 (2011) 99–107.
[8] A. Sheidaei, X. Xiao, X. Huang, J. Wang, Mechanical characterization of a lithium ion battery separator using a dynamic mechanical analyzer, SAE Techni Paper, 2011.
[9] J. Nunes-Pereira, C.M. Costa, R. Leones, M.M. Silva, S. Lanceros-Méndez, Li-ion battery separator membranes based on poly(vinylidene fluoride-trifluoroethylene)/carbon nanotube composites, Solid State Ionics 249–250 (2013) 63–71.
[10] A. Gören, C.M. Costa, M.N. Tamaño Machiavello, D. Cíntora-Juárez, J. Nunes-Pereira, J.L. Tirado, et al., Effect of the degree of porosity on the performance of poly(vinylidene fluoride-trifluoroethylene)/poly(ethylene oxide) blend membranes for lithium-ion battery separators, Solid State Ionics 280 (2015) 1–9.
[11] J.S. Park, S.J. Gwon, Y.M. Lim, Y.C. Nho, Influence of the stretching temperature on an alumina filled microporous high density polyethylene membrane, Mater. Des. 31 (2010) 3215–3219.
[12] J. Purewal, J. Wang, J. Graetz, S. Soukiazian, H. Tataria, M.W. Verbrugge, Degradation of lithium ion batteries employing graphite negatives and nickel–cobalt–manganese oxide plus spinel manganese oxide positives: part 2, chemical–mechanical degradation model, J. Power Sources 272 (2014) 1154–1161.
[13] T. Yamaguchi, S. Koda, Mode-coupling theoretical analysis of transport and relaxation properties of liquid dimethylimidazolium chloride, J. Chem. Phys. 132 (2010).
[14] C.Z. Man, P. Jiang, K.W. Wong, Y. Zhao, C.Y. Tang, M.K. Fan, et al., Enhanced wetting properties of a polypropylene separator for a lithium-ion battery by hyperthermal hydrogen induced cross-linking of poly(ethylene oxide), J. Mater. Chem. A 2 (2014) 11980–11986.
[15] Edith A. Turi, Thermal Characterization of Polymeric Materials, Academic Press, 1981.
[16] C.T. Love, Thermomechanical analysis and durability of commercial micro-porous polymer Li-ion battery separators, J. Power Sources 196 (2011) 2905–2912.
[17] T.-H. Cho, M. Tanaka, H. Onishi, Y. Kondo, T. Nakamura, H. Yamazaki, et al., Battery performances and thermal stability of polyacrylonitrile nano-fiber-based nonwoven separators for Li-ion battery, J. Power Sources 181 (2008) 155–160.
[18] T.-H. Cho, M. Tanaka, H. Ohnishi, Y. Kondo, M. Yoshikazu, T. Nakamura, et al., Composite nonwoven separator for lithium-ion battery: development and characterization, J. Power Sources 195 (2010) 4272–4277.
[19] J. Nunes-Pereira, C.M. Costa, S. Lanceros-Mendez, Polymer composites and blends for battery separators: state of the art, challenges and future trends, J. Power Sources 281 (2015) 378–398.
[20] C.M. Costa, M.M. Silva, S. Lanceros-Mendez, Battery separators based on vinylidene fluoride (VDF) polymers and copolymers for lithium ion battery applications, RSC Adv. 3 (2013) 11404–11417.
[21] J. Cannarella, X.Y. Liu, C.Z. Leng, P.D. Sinko, G.Y. Gor, C.B. Arnold, Mechanical properties of a battery separator under compression and tension, J. Electrochem. Soc. 161 (2014) F3117–F3122.
[22] K.Y. Oh, J.B. Siegel, L. Secondo, S.U. Kim, N.A. Samad, J.W. Qin, et al., Rate dependence of swelling in lithium-ion cells, J. Power Sources 267 (2014) 197–202.
[23] J. Chen, Roles of Bider and Separator Mechanical Behaviors in the Lithium-ion Battery Ageing and Safety Harbin Institute of Technology, 2014.
[24] S. Yan, X. Xiao, X. Huang, X. Li, Y. Qi, Unveiling the environment-dependent mechanical properties of porous polypropylene separators, Polymer 55 (2014) 6282–6292.
[25] J. Liu, V.P.W. Shim, Characterization and modelling of in-situ La-based bulk metallic glass composites under static and dynamic loading, Int. J. Impact Eng. 80 (2015) 94–106.
[26] J. Xu, B.H. Liu, L.B. Wang, S. Shang, Dynamic mechanical integrity of cylindrical lithium-ion battery cell upon crushing, Eng. Fail. Anal. 53 (2015) 97–110.
[27] J.C. Chen, Y.D. Yan, T. Sun, Y. Qi, X.D. Li, Deformation and fracture behaviors of microporous polymer separators for lithium ion batteries, RSC Adv. 4 (2014) 14904–14914.
[28] J. Feng, W.B. Li, X.M. Wang, M.L. Song, H.Q. Ren, W.B. Li, Dynamic spherical cavity expansion analysis of rate-dependent concrete material with scale effect, Int. J. Impact Eng. 84 (2015) 24–37.
[29] V. Singh, A. Misra, R. Parthasarathy, Q. Ye, P. Spencer, Viscoelastic properties of collagen-adhesive composites under water-saturated and dry conditions, J. Biomed. Mater. Res. A 103 (2015) 646–657.
[30] ASTM, Standard test method for tensile properties of plastics1. 100 Barr Harbor Drive, West Conshohocken, PA 19428-2959, United States, 2016.